were washed with 0.1% (w/v) saponin in phosphate-buffered saline and then eluted with 0.1 M glycine (pH 2.5).
22. I. S. Näthke *et al.*, *Cell* **68**, 899 (1992).
23. A cytosolic extract from [^{35}S]methionine-labeled HeLa cells (*5*) was incubated with GST, GST-β3A$_H$, or GST-β3A$_C$ coupled to Affi-Gel 15 beads. Bound proteins were eluted by heating the beads at 95°C for 5 min in the presence of 1% (w/v) SDS, 10 mM dithiothreitol, 0.1 M tris-HCl (pH 7.4). Samples were diluted 1:20 with 50 mM tris-HCl buffer (pH 7.4) containing 1% (w/v) Triton X-100, 0.3 M NaCl, 10 mM iodoacetamide, 5 mM EDTA, 0.1% (w/v) BSA and immunoprecipitated (*5*) with the X22 antibody [F. M. Brodsky, *J. Cell Biol.* **101**, 2047 (1985)].
24. A cDNA fragment encoding residues 1 to 579 of human clathrin heavy chain was engineered by PCR for cloning into the Bam HI–Xho I sites of the pBluescript SK II vector (Stratagene). In vitro transcription-translation was performed in the presence of [^{35}S]methionine using the TNT system (Promega). The translated products were diluted 1:10 in 50 mM Hepes buffer (pH 7.4) containing 0.1 M KCl, 2 mM $MgCl_2$, 0.1 mM $CaCl_2$, 10% (v/v) glycerol, 0.1% (w/v) BSA, and 0.05% (w/v) Triton X-100 and centrifuged at 120,000*g* for 30 min at 4°C to remove protein aggregates.
25. J. W. Slot, H. J. Geuze, Gigengack, S., G. E. Lienhard, D. E. James, *J. Cell Biol.* **113**, 123 (1991).
26. We thank M.-C. Fournier and V. Oorschot for excellent technical assistance; L. Green and E. Eisenberg for advice on the purification of clathrin; F. Brodsky, L. Samelson, E. Ungewickell, and W. Zhang for generous gifts of reagents; and J. Donaldson, J. Lippincott-Schwartz, C. E. Ooi, and G. Storz for critical review of the manuscript.

12 December 1997; accepted 17 February 1998

NMR Structure of a Classical Pseudoknot: Interplay of Single- and Double-Stranded RNA

Michaël H. Kolk, Marinette van der Graaf,* Sybren S. Wijmenga,† Cornelis W. A. Pleij,‡ Hans A. Heus, Cornelis W. Hilbers§

Pseudoknot formation folds the 3′ ends of many plant viral genomic RNAs into structures that resemble transfer RNA in global folding and in their reactivity to transfer RNA–specific proteins. The solution structure of the pseudoknotted T arm and acceptor arm of the transfer RNA–like structure of turnip yellow mosaic virus (TYMV) was determined by nuclear magnetic resonance (NMR) spectroscopy. The molecule is stabilized by the hairpin formed by the 5′ end of the RNA, and by the intricate interactions related to the loops of the pseudoknot. Loop 1 spans the major groove of the helix with only two of its four nucleotides. Loop 2, which crosses the minor groove, interacts closely with its opposing helix, in particular through hydrogen bonds with a highly conserved adenine. The structure resulting from this interaction between the minor groove and single-stranded RNA at helical junctions displays internal mobility, which may be a general feature of RNA pseudoknots that regulates their interaction with proteins or other RNA molecules.

RNA pseudoknots are found in virtually all classes of RNA and play key roles in a variety of biological processes. They often constitute a local structural element that may act as a recognition site for proteins involved in replication initiation or translational regulation (*1*). The formation of most functional pseudoknots involves Watson-Crick base pairing of residues in an RNA hairpin loop with nucleotides outside that loop, yielding two stems that are mutually connected by two nonequivalent loops. Stacking of these helical segments is thought to add to the overall stability of the pseudoknot and represents a major feature of the functional pseudoknots described to date (*2*–*4*). Consistent with the RNA A-helical geometry, the connecting loops 1 and 2 are always located on opposite sides of the helix, at the major and minor groove side, respectively; however, detailed information on tertiary structure in the pseudoknot and on the determinants of its stability has not been available.

Here we describe the NMR structure of a pseudoknotted fragment that was resolved at an atomic level in all regions, allowing an accurate description of the interplay of single- and double-stranded regions responsible for the distinct structural and dynamic properties of the molecule. The system matches the complete T arm and valine acceptor arm of the tRNA-like structure of TYMV genomic RNA (Fig. 1A). This structure was the earliest example found of this class of pseudoknot motifs (*5*, *6*), which is present in the genomic RNAs of many plant viruses (*7*). The tRNA mimicry is achieved through pseudoknot formation in the aminoacyl acceptor arm, which leads to a global folding of the entire tRNA-like structure into an L-shaped molecule, despite a secondary structure that is very different from tRNA (*6*, *8*). The structural resemblance to tRNA is also evident from its reactivity to tRNA-specific enzymes, such as cleavage by ribonuclease (RNase) P and aminoacylation by valyl-tRNA synthetase, as in the case of TYMV genomic RNA (*7*, *9*).

The 44-nucleotide RNA molecule we studied is identical to the 3′-terminal region of TYMV RNA, with the exception of some structurally silent alterations in the stem and loop of the hairpin at the 5′ side of the acceptor arm (*10*), which is required to seal down an otherwise unstable pseudoknot (*11*). The size of the molecule required the use of both uniformly and selectively (A-only and U-only) ^{13}C- and ^{15}N-labeled samples for the NMR structure determination (*12*). Selective labeling proved essential for assigning the resonances of loop residues and of residues located near the helical junction sites, some of which are severely broadened (Fig. 1B). We could identify most resonances with standard triple-resonance techniques, but some additional experiments were needed for complete assignment of the sugar-spin systems (*13*). Distance and dihedral restraints derived from the NMR data were used for structure calculations (*14*) to obtain the final ensemble of 10 structures (Table 1 and Fig. 2).

The average structure shows an A-type helical conformation for all three stem regions. Colinearity is maintained at both helical junction sites. Slight torsional and swaying motions between these helices on a millisecond time scale are most likely responsible for the observed line broadening for residues near the interface of stems 1 and 2. Changes in the ring-current effects resulting from even a modest dislocation of an aromatic moiety can result in a significant change in the chemical shift of nearby protons (*15*), even if the latter themselves are within a stable Watson-Crick base pair. This type of dynamics probably also accounts for similar line broadening reported for a different pseudoknot (*3*), and we expect it to be a general phenomenon of this class of RNA motifs.

The rod-shaped molecule is capped by a seven-membered loop that is comparable to the T loop in tRNA. Although two mutations were introduced at the 5′ side of the loop, its sequence contains all the

Nijmegen SON Research Center for Molecular Structure, Design and Synthesis, Laboratory of Biophysical Chemistry, University of Nijmegen, Toernooiveld, 6525 ED Nijmegen, The Netherlands.

*Present address: Department of Radiology, University Hospital Nijmegen, 6500 HB Nijmegen, The Netherlands. †Present address: Department of Medical Biochemistry and Biophysics, University of Umeå, S901 87, Sweden. ‡Present address: Leiden Institute of Chemistry, University of Leiden, 2300 RA Leiden, The Netherlands. §To whom correspondence should be addressed.

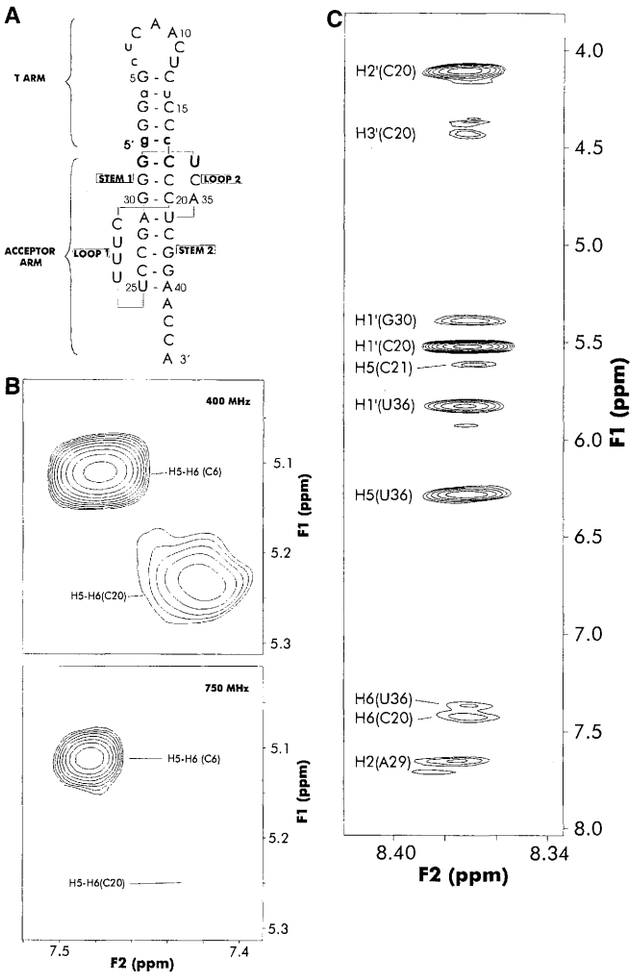

Fig. 1. (**A**) Secondary structure of the T arm and pseudoknotted acceptor arm of the tRNA-like structure of TYMV genomic RNA. Lowercase letters are non–wild-type residues. (**B**) Example of the line broadening observed for residues near the junction site of the pseudoknot. The nuclear Overhauser effect (NOE) crosspeak between the H-5 and H-6 resonances of C20, which is still visible at 400 MHz, is broadened beyond the level of detection at 750 MHz as a result of conformational averaging. The H-5 to H-6 NOE crosspeak of C6 is displayed as a reference. (**C**) Strip taken from a 200-ms NOESY experiment at 400 MHz showing the long-range NOEs to the A35 H-2 resonance. F1 and F2 are the frequencies in the first and second dimensions, respectively.

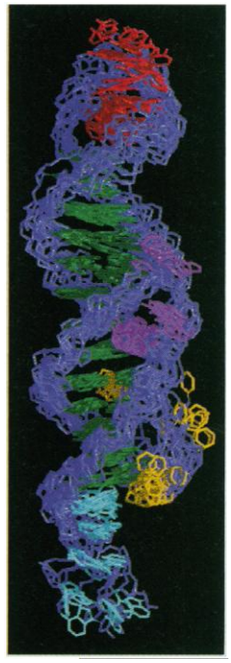

Fig. 2. Best overall superposition of the 10 simulated annealing structures (⟨SA⟩) of the TYMV pseudoknot; only the heavy atoms are shown. The RNA backbone is colored blue and bases are color-coded by domain: stem residues in green, the T loop in red, loop 1 in yellow, loop 2 in magenta, and the 3′ ACCA tail in cyan. All color figures were generated with MOLMOL (*28*).

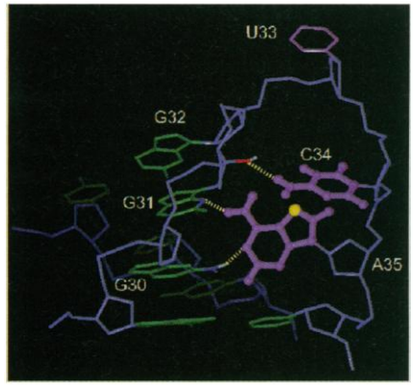

Fig. 3. Detail of the structure showing the hydrogen bonds found between loop 2 and stem 1 (see text). The highly DEPC-reactive N-7 atom of A35 is highlighted in yellow.

invariable residues of valine-accepting plant viral tRNA-like structures (*7*). The loop has a well-defined structure governed by a classical U-turn, as observed in the tRNA anticodon loop, and is almost identical to the NMR structure of the initiator $tRNA^{Met}$ anticodon loop (*16*). Although it is not experimentally proven, we expect that this loop interacts with the D loop analog in the tRNA-like structure in a manner similar to that in tRNA. Clearly, the outwardly turned residues A9 through U12 are all fixed in a suitable orientation for such an interaction. However, the conserved sequence of the "T loop" in plant viral RNAs allows for a loop composition that has been shown to be a very flexible structure (*17*). Therefore, a well-defined structure in the isolated "T loop" does not seem to be required for any interactions with the "D loop" region in tRNA-like structures.

We found unexpected conformations in the loop regions of the pseudoknot. NMR data from other pseudoknots (*2*, *3*) and computer modeling based on biochemical data (*18*) have led to the assumption that, in general, the size of the minor groove in RNA does not permit any interactions with the bases in loop 2, which should therefore be ill-defined and exposed toward the solvent. In the present structure, to the contrary, loop 2 interacts with the minor groove of stem 1 and adopts a distinct conformation, not been previously observed, around residue A35 (Fig. 3). This residue is very well defined, as is apparent from the large number of long-range NOEs to its H-2 proton (Fig. 1C). Its base is tilted to an angle of almost 90° with respect to the plane of the opposing base pairs, allowing it to hydrogen bond to both G30 and G31: from N-1 of A35 to the amino group of G30 and from the A35 amino group to the N-3 of G31. In addition, the full ensemble of structures suggests that residue C34, which stacks on A35, is somewhat flexible, and that its amino protons can be within hydrogen-bonding distance of the 2′OH of G31. These three hydrogen bonds form a helix-to-loop triple-strand interaction in an RNA pseudoknot, which has not been previously observed. They anchor the base of A35 deep within the minor groove and unite loop 2 with its opposing helix. They also may provide the energetical compensation for the conformational strain in the loop, manifested by the unusual S-type sugar conformation of residues A35 and U33.

The strong conservation of the adenine at position 35 among many plant viral RNAs containing valine-accepting tRNA-

like structures (*19*) is explained by the position of this residue in the NMR structure. The uncommon tilting of its base moiety seems to be the only way to allow for triple interactions without affecting the overall direction of the chain in loop 2, which would impose unfavorable strain on C34 and U33. Given this orientation, the N-6 amino group is essential as a hydrogen-bond donor to G31, a requirement that can only be fulfilled by an adenine. Although the particular conformation around A35 has not been reported before, there are several other examples of adenines that hydrogen bond to the minor groove of RNA helices (*20*), suggesting a general principle of such adenine-related interactions involved in the formation of higher order structure in RNA molecules.

The prominent reactivity of residue A35 toward diethylpyrocarbonate (DEPC) has been regarded as compelling evidence for an outwardly turned orientation of its base (*18*), which would contradict the NMR structure. However, the adenine N-7, which is the actual site of modification in DEPC treatment, is still fully exposed toward solvent in the present NMR structure (Fig. 3), which is consistent with the chemical reactivity. Moreover, the mentioned triple interactions are expected to maintain structural integrity around this location even at higher temperatures, concurrent with the overall stability of the pseudoknot (*21*). This offers an explanation for the fact that the high relative DEPC reactivity for this residue is independent of temperature (*18*).

At the opposite side of the pseudoknot's quasi-continuous helix, loop 1 bridges the gap between C20 and U25 over the major groove of stem 2 (Fig. 4). From model-building studies (*18*) it has been proposed that this loop is made up of residues C21 through U23 in a stacked orientation, whereas the helical course of stem 2 is extended by U24 stacking on U25, which would allow for a Watson-Crick base pair between U24 and A41. Our data confirm that U24 stacks on U25 but also show that U24 is not involved in base pairing. Furthermore, continued stacking of U23 on U24 reduces the remaining distance over the major groove to about 11 Å, which can be easily spanned by the remaining loop residues C21 and U22. A number of atypical torsion angles of U22—with γ in the *trans*-region and a pure S-type sugar pucker—indicate that this residue is fully extended, allowing C21 enough conformational freedom to partly stack on C20. The unusual orientation of U22 is further evidenced by the strong downfield shifts of its sugar ^{1}H and ^{13}C resonances.

The A-helical facade of the molecule is not disturbed by either of the pseudoknot loops (Fig. 2). The major groove of stem 2 can easily accommodate C21 and U22, whereas tertiary interactions deeply bury the residues of loop 2 into the minor groove of stem 1, preventing any residue from bulging out of the helical coil. The system can therefore structurally be regarded as the counterpart of the T arm and acceptor arm in tRNA, which can explain the recognition of the acceptor stem by aminoacyl tRNA synthetases. In the case of valyl-tRNA synthetase this is easily understood because this enzyme belongs to the class I synthetases, which bind to the minor groove side of the acceptor helix, close to the extended 3′ ACCA tail. Comparison of the present structure with the x-ray structure (*22*) of $tRNA^{Glu}$ complexed with its cognate synthetase (also belonging to class I) reveals that the two pseudoknot loops are at the side opposite from where the enzyme docks. Binding of aminoacylating enzymes to the TYMV acceptor arm is not limited to the minor groove side, however, because the acceptor arm of TYMV can be mischarged by histidinyl-tRNA synthetase (*23*), which belongs to the major groove–binding, class II synthetases. Docking of such an enzyme conceivably displaces loop 1 from its native location in the major groove of stem 2, thereby disturbing the base-base stacking interactions of U23 and U24. The energy cost of this displacement is expected to be limited, however, because no hydrogen bonds need to be broken and the native structure is already somewhat flexible at this site, as evidenced by the larger line widths and higher local root-mean-square deviations for these residues. Thus, it appears that the structure found for loop 1 does not contribute as much to the stability and functionality of the molecule as does the structure of loop 2. The observation that deleting three of four

Table 1. Structural statistics. ⟨SA⟩ denotes the final ensemble of 10 simulated-annealing structures, ⟨$\overline{SA}$⟩ is the average structure, ⟨$\overline{SA}$⟩$_r$ the average structure after minimization of restrained energy, SD the standard deviation, and rmsd the root-mean-square deviation.

Parameter	⟨SA⟩ ± SD	⟨$\overline{SA}$⟩$_r$
Rmsd (Å/degree)		
Distance restraints (451)*	0.085 ± 0.003	0.074
Dihedral restraints (257)	2.918 ± 0.989	0.756
Rmsd from idealized geometry		
Bonds (Å)	0.0094 ± 0.0004	0.0084
Angles (degrees)	1.957 ± 0.110	1.815
Impropers (degrees)	1.055 ± 0.026	1.034
Restraint violations		
Number of distance violations† > 0.4 Å	4 ± 1	2
Number of dihedral violations > 5°	5 ± 2	0

Parameter	⟨SA⟩ vs. ⟨$\overline{SA}$⟩ ± SD	⟨SA⟩ vs. ⟨$\overline{SA}$⟩$_r$ ± SD
Atomic rmsd (Å)‡		
All	2.10 ± 0.23	2.55 ± 0.35
Loop regions§	0.99 ± 0.28	1.20 ± 0.31

* Internucleotide and conformationally relevant intranucleotide NOE restraints. †⟨SA⟩ does not contain any violations >0.5 Å. None of the violations clusters at a particular site of the molecule or shows any persistency within the ensemble. ‡Heavy atoms only. §Average values of the local rmsd's for residues 6 through 12, 21 through 24, and 33 through 35.

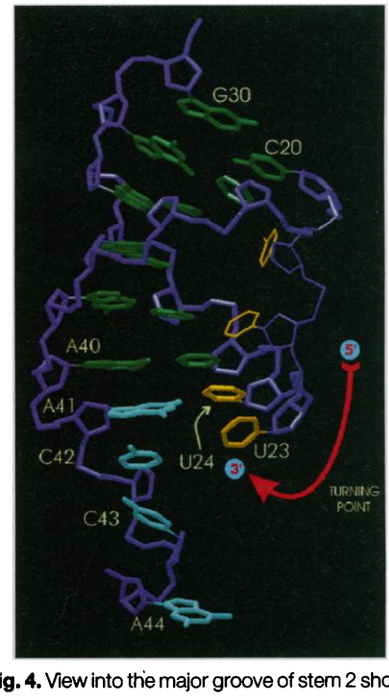

Fig. 4. View into the major groove of stem 2 showing the distinct turn in loop 1. The coloring scheme is identical to that of Fig. 2. U24 and U23 are not involved in base-pairing interactions with the opposite bases of A41 and C42. Nucleotides C21 and U22, spanning the major groove, are drawn in thin lines. The curved arrow denotes the direction of the RNA chain.

residues in loop 1 is not detrimental to pseudoknot stability (*24*) strongly supports this hypothesis.

Typically, the TYMV pseudoknot presents itself as a region of high structural integrity, potentially offering a number of recognition sites to proteins involved in replication initiation of the viral genome. Unlike other structural elements such as most RNA hairpins, it does so without being a solid and impenetrable body. Rather, the pseudoknot has a predisposition for partial unfolding that may very well be of functional significance. This "soft" characteristic of the structure is reflected by the observed twisting and swinging motions of the helical segments and the requirement for the T arm to prevent the slipping of strands in the pseudoknot. The difference in structural perseverance of the molecule as compared with tRNA could relate to its function in RNA replication, in which it should not obstruct the formation of the replication initiation complex or the elongation of the minus strand by the replicase. Recent in vitro studies suggested that the long quasi-continuous helix of the pseudoknot enables an optimal interaction with both the replicase and the valyl-tRNA synthetase, while not obstructing the replicase in its elongation mode (*25*). A comparable role has been hypothesized for pseudoknots involved in frame-shifting activity (*26*) and may be applicable to other functional pseudoknots.

REFERENCES AND NOTES

1. E. ten Dam, C. W. A. Pleij, D. Draper, *Biochemistry* **31**, 1665 (1992); C. W. A. Pleij, *Curr. Opin. Struct. Biol.* **4**, 337 (1994).
2. J. D. Puglisi, J. R. Wyatt, I. Tinoco Jr., *J. Mol. Biol.* **214**, 437 (1990).
3. L. X. Shen and I. Tinoco Jr., *ibid.* **247**, 963 (1995).
4. Z. Du, D. Giedroc, D. Hoffman, *Biochemistry* **35**, 4187 (1996).
5. M. Pinck, P. Yot, F. Chapeville, H. M. Duranton, *Nature* **226**, 954 (1970); P. Yot, M. Pinck, A. L. Haenni, H. M. Duranton, F. Chapeville, *Proc. Natl. Acad. Sci. U.S.A.* **67**, 1345 (1970).
6. K. Rietveld, R. Van Poelgeest, C. W. A. Pleij, J. H. Van Boom, L. Bosch, *Nucleic Acids Res.* **10**, 1929 (1982).
7. R. M. W. Mans, C. W. A. Pleij, L. Bosch, *Eur. J. Biochem.* **201**, 303 (1991).
8. C. Florentz *et al.*, *EMBO J.* **2**, 269 (1982).
9. T. C. Hall, *Int. Rev. Cytol.* **60**, 1 (1979).
10. A. Van Belkum *et al.*, *Eur. J. Biochem.* **183**, 591 (1989).
11. Structure-probing experiments in which enzymatic digestion was done with RNase T1 and nuclease S1 {essentially as described [A. V. Van Belkum, P. Verlaan, J. B. Kun, C. W. A. Pleij, L. Bosch, *Nucleic Acids Res.* **16**, 1931 (1988)]} confirmed the secondary structure presented in Fig. 1A. Fragments lacking the 5′ hairpin (residues 1 to 17) showed a different protection pattern for the pseudoknot, indicating an unstable structure under native conditions (M. H. Kolk *et al.*, data not shown).
12. T7 RNA polymerase was used to synthesize RNA fragments by in vitro transcription [J. F. Milligan, D. R. Groebe, G. W. Witherell, O. C. Uhlenbeck, *Nucleic Acids Res.* **15**, 8783 (1987)], with linearized plasmid as a template (*10*). The RNA was purified with a Q-Sepharose column and preparative polyacrylamide gel electrophoresis. Nucleoside triphosphates were labeled with ^{13}C and ^{15}N as described [E. Nikonowicz *et al.*, *Nucleic Acids Res.* **20**, 4507 (1992)]. For the A-only labeled sample, [^{13}C, ^{15}N]adenosine triphosphate was separated from other nucleotides before synthesis, also with a Q-Sepharose column. The U-only sample was prepared with commercially obtained [^{13}C, ^{15}N]uridine monophosphate (Cambridge Isotope Laboratories), which was enzymatically converted to uridine triphosphate. Because the pseudoknot structure depends on the presence of Mg^{2+}, the purified RNA samples were dialyzed against a 10 mM $MgCl_2$ solution at pH 6.7 and concentrated to 500 μl with a Centricon microconcentrator. Sample concentrations were between 1 and 2.5 mM.
13. NMR spectra were collected on Bruker AM400 and AMX/DRX600 and on Varian Unity+ 500 and 750 spectrometers. Exchangable protons were assigned from a nuclear Overhauser effect spectroscopy (NOESY)–jr experiment [P. Plateau and M. Guéron, *J. Am. Chem. Soc.* **104**, 7310 (1982)] and a through-bond connectivity experiment optimized for uridines [J. P. Simorre, G. R. Zimmermann, A. Pardi, B. T. Farmer, L. Mueller, *J. Biomol. NMR* **6**, 427 (1995)]. Nonexchangable protons were assigned with 2D NOESY [J. Jeener, B. H. Meier, P. Bachmann, R. R. Ernst, *J. Chem. Phys.* **71**, 4546 (1979)], total correlation spectroscopy (TOCSY) [C. Griesinger, G. Otting, K. Wüthrich, R. R. Ernst, *J. Am. Chem. Soc.* **110**, 7870 (1988)], NOESY–heteronuclear multiple-quantum coherence (HMQC) and HMQC-NOESY [M. Ikura, L. E. Kay, R. Tschudin, A. Bax, *J. Magn. Reson.* **86**, 204 (1990)], doubly X-filtered 2D NOESY [R. H. A. Folmer, C. W. Hilbers, R. N. H. Konings, K. Hallenga, *J. Biomol. NMR* **5**, 427 (1995)], and HCCH-TOCSY [A. Bax, G. M. Clore, A. M. Gronenborn, *J. Magn. Reson.* **88**, 425 (1990); P. Legault, B. T. Farmer, L. Mueller, A. Pardi, *J. Am. Chem. Soc.* **116**, 2203 (1994)]. Several new applications had to be developed to tackle the specific assignment problems of this system and to obtain the necessary torsion angle restraints. We assigned ^{31}P resonances from a ^{31}P–constant time (CT)–^{13}C-^{1}H experiment using gradient enhancement for the ^{13}C dimension [L. E. Kay, P. Keifer, T. Saarinen, *J. Am. Chem. Soc.* **114**, 10663 (1992)]. Dihedral angles were determined from gradient-enhanced, CT-TOCSY-HSQC and {^{31}P} spin-echo difference experiments [G. W. Vuister, A. C. Wang, A. Bax, *ibid.* **115**, 5334 (1993); P. Legault, F. M. Jucker, A. Pardi, *FEBS Lett.* **362**, 156 (1995)]. Details of these experiments will be reported elsewhere.
14. Interproton distance restraints were derived from crosspeak volumes in 80-, 150-, and 200-ms NOESY spectra (recorded at 30°C) and were given ±20% error bounds. Crosspeaks that were only observable at longer mixing times were corrected for spin diffusion by using the H-5 to H-6 NOE as a reference for short distances (2.45 Å) and helical intraresidue H-1′ to H-6 or H-8 NOE for longer distances (3.65 Å) [I. L. Barsukov and L.-Y. Lian, in *NMR of Macromolecules. A Practical Approach*, G. Roberts, Ed. (Oxford Univ. Press, New York, 1993), pp. 315–357]. NOEs taken from three-dimensional (3D) experiments were subdivided into four classes: strong (1.8 to 3.0 Å), medium (2.5 to 3.5 Å), weak (3.0 to 6.0 Å), and very weak (4.0 to 7.0 Å). Distance restraints relating to exchange-broadened NOEs were determined separately and collected exclusively from spectra recorded at 400 MHz. Calibration was based on NOE intensities of proton pairs, with fixed distances of the involved residues. All NOEs that could not be properly integrated because of overlap were assigned bounds of 1.8 to 7.0 Å. Watson-Crick hydrogen-bonding and planarity restraints were imposed for residues present in a regular A helix on the basis of the imino spectra and the observed NOEs and chemical shifts. For the intraresidue restraints, only the conformationally relevant aromatic-to-sugar proton distances were used. We assigned sugar puckers as N- or S-type conformations, using dihedral restraints, in the case of weak or strong H-1′ to H-2′ crosspeak intensities, respectively, as observed in 2D and ^{13}C-edited 3D TOCSY experiments. The angles around α and ζ were restrained to 0° ± 120° for all residues but C8 and A44, which have ^{31}P resonances that are clearly shifted from the A-helical values and were therefore left unconstrained. Aromatic to H-1′, H-2′, or H-3′ proton NOEs indicated that all χ angles are in the anti-range, which were therefore set to −158° ± 60°. Other torsion angle restraints were set to the determined value ± 30°. We used 451 experimental distance restraints (258 sequential and 193 intraresidue) and 257 pucker and dihedral angle restraints as input in a torsion-angle dynamics protocol (*27*) using X-PLOR V3.851 [A. T. Brünger, *X-PLOR. A System for X-ray Crystallography and NMR* (Yale Univ. Press, New Haven, CT, 1992)]. This protocol was largely identical to that proposed for a DNA duplex (*27*). Out of the 100 structures that were calculated starting from a random extended conformation, ~50% had the correct secondary structure, and ~80% of those converged to the same conformation for the central part of the molecule (around stem 1 and loop 2). Because these structures contained some residual restraint violations, 14 of those were selected on the basis of lowest energies for a subsequent round of conventional simulated annealing (SA), which included a 60-ps molecular dynamics run of 20,000 steps at 2000 K, followed by gradual cooling during 30 ps to 300 K in 10,000 steps. Force constants for NOE restraints were entered as soft-square well potentials at 50 kcal mol^{-1} $Å^{-2}$. Dihedral restraints were introduced with an initial force constant of 5 kcal mol^{-1} rad^{-2} during the high-temperature dynamics, which was increased to 200 kcal mol^{-1} rad^{-2} at the beginning of the cooling step. The average structure ($\langle\overline{SA}\rangle$) was determined from the 10 structures with the lowest energies and restraint violations out of the ensemble of 140 structures thus calculated and subjected to 6000 steps of restrained conjugate gradient energy minimization.
15. S. S. Wijmenga, M. Kruithof, C. W. Hilbers, *J. Biomol. NMR* **10**, 337 (1997).
16. D. C. Schweisguth and P. B. Moore, *J. Mol. Biol.* **267**, 505 (1997).
17. L. J. Yao, T. L. James, J. T. Kealey, D. V. Santi, U. Schmitz, *J. Biomol. NMR* **9**, 229 (1997).
18. P. Dumas *et al.*, *J. Biomol. Struct. Dyn.* **4**, 707 (1987).
19. To our knowledge, 17 pseudoknots have been described that are located at comparable positions in the valine-accepting tRNA-like structures found in tymo-, tobamo-, and furoviruses. All but one of these have an adenine at position 35. Hydrogen-bonding partners G30 and G31 are less strongly conserved throughout these species, being AG, GC, or AC in 7 out of 17 sequences. The anatomy of the possible tertiary interactions for these cases remains to be established.
20. M. Chastain and I. Tinoco Jr., *Biochemistry* **32**, 14220 (1993); J. H. Cate *et al.*, *Science* **273**, 1678 (1996); H. W. Pley, K. M. Flaherty, D. B. McKay, *Nature* **372**, 111 (1994).
21. Chemical shifts and NOEs pertaining to A35 remain unaffected in a temperature range from 5° to 40°. Imino proton resonances of the pseudoknot broaden considerably at temperatures above 50°.
22. M. A. Rould, J. J. Perona, T. A. Steitz, *Nature* **352**, 213 (1991).
23. J. Rudinger, C. Florentz, T. Dreher, R. Giegé, *Nucleic Acids Res.* **20**, 1865 (1992).
24. R. M. W. Mans, C. Guerrier-Takada, S. Altman, C. W. A. Pleij, *ibid.* **18**, 3479 (1990).
25. B. A. L. M. Deiman, A. K. Koenen, P. W. G. Verlaan, C. W. A. Pleij, *J. Virol.*, in press.

26. P. Schimmel, *Cell* **58**, 9 (1989); I. Brierley, *J. Gen. Virol.* **76**, 1885 (1995).
27. E. G. Stein, L. M. Rice, A. T. Brünger, *J. Magn. Reson.* **124**, 154 (1997).
28. R. Koradi, M. Billeter, K. Wüthrich, *J. Mol. Graphics* **14**, 51 (1996).
29. The NMR experiments were performed at the SON Large Scale NMR facility (Nijmegen and Utrecht, The Netherlands). This research was supported by the Netherlands Foundation of Chemical Research (SON) and the Dutch Life Science Foundation, with financial aid from the Netherlands Organization of Scientific Research. H.A.H. was supported by a grant from the Royal Netherlands Academy of Arts and Sciences. We wish to thank J. Joordens for technical assistance.

4 December 1997; accepted 24 February 1998

Autoinducer of Virulence As a Target for Vaccine and Therapy Against *Staphylococcus aureus*

Naomi Balaban,* Tzipora Goldkorn, Rachael T. Nhan, Luong B. Dang, Steven Scott, Rose M. Ridgley, Avraham Rasooly, Susan C. Wright, James W. Larrick, Reuven Rasooly, James R. Carlson

Staphylococcus aureus causes pathologies ranging from minor skin infections to life-threatening diseases. Pathogenic effects are largely due to production of bacterial toxin, which is regulated by an RNA molecule, RNAIII. The *S. aureus* protein called RAP (RNAIII activating protein) activates RNAIII, and a peptide called RIP (RNAIII inhibiting peptide), produced by a nonpathogenic bacteria, inhibits RNAIII. Mice vaccinated with RAP or treated with purified or synthetic RIP were protected from *S. aureus* pathology. Thus, these two molecules may provide useful approaches for the prevention and treatment of diseases caused by *S. aureus*.

Staphylococcus aureus is a Gram-positive bacterial pathogen that causes diseases ranging from minor skin infections to life-threatening deep infections such as pneumonia, endocarditis, meningitis, postoperative wound infections, septicemia, and toxic shock syndrome (*1*). Hospitalized patients are at particular risk; over 500,000 nosocomial infections are reported per year (*2*). The emergence of drug resistance has made many of the available antimicrobial agents ineffective. Therefore, alternative methods for prevention and treatment of bacterial infections in general and of *S. aureus* infections in particular are eagerly sought.

Like other Gram-positive bacteria, *S. aureus* causes diseases chiefly by production of virulence factors such as hemolysins, enterotoxins, and toxic shock syndrome toxin. The synthesis of virulence factors in *S. aureus* is controlled by a regulatory RNA molecule, RNAIII (*3–5*), encoded by the *agr* locus. The *rnaiii* gene is transcribed in culture only from the mid-exponential phase of growth and is autoinduced by the RNAIII activating protein (RAP) (*6*). RAP is continuously secreted by the bacteria and activates *rnaiii* only at a concentration threshold (*6*). Antibodies to RAP block the activation of *rnaiii* in vitro. A peptide, termed RNAIII inhibiting peptide (RIP), is produced by a nonpathogenic strain of *S. aureus* mutated by nitrosoguanidine (*6*). RIP competes with RAP for activation of *rnaiii* and thus inhibits production of toxin by *S. aureus* (*6*). This suggests that interference with activation of the *agr* system by blocking the autoinducer RAP or by supplying RIP may inhibit the expression of all toxins regulated by *rnaiii*, thereby interfering with pathogenesis. We report that mice vaccinated with RAP or treated with RIP are protected from *S. aureus* infection.

We purified RAP from postexponential supernatants of wild-type *S. aureus* (Fig. 1) as described (*6*) and the peak fraction (Fig. 1, B and C) contained a protein of about 38 kD (Fig. 1D). We also purified RAP from postexponential supernatants of an *agr*-null strain in which the entire *agr* locus was replaced with the *tetM* marker (*7*) (Fig. 1, B and D), which suggests that RAP is independent of *agr*.

To test whether immunization with RAP can inhibit *S. aureus* infection, we used the murine model of cutaneous infection (*8*). When the wild-type Smith diffuse (SD) strain of *S. aureus* is injected subcutaneously together with dextran beads (Cytodex), a visible, measurable lesion (cellulitis) is induced after 24 hours. In contrast, no lesion is induced in animals injected with Cytodex beads alone (*9*).

Mice were vaccinated (*10*) with RAP purified (*6*) from an *agr*-null strain (RAP*) or from a wild-type *S. aureus* strain (RAP) (*9*) (Table 1). After they were challenged with *S. aureus*, 72% (24 of 33) of RAP-vaccinated mice remained free of disease compared with 30% (3 of 10) of control mice immunized with complete Freund's adjuvant (CFA) and none of the untreated controls. This difference was statistically significant (Fisher's exact

Table 1. Vaccination or suppression of *S. aureus* SD infections (*10, 16*).

Treatment group	No. of mice	No lesions		Lesions		Death	
		n	(%)	*n*	Mean size (mm^2)	*n*	(%)
Vaccination with RAP as an antigen							
RAP	24	17	(71)	6	96	1	(4)
RAP*	9	7	(78)	2	84	0	(0)
CFA	10	3	(30)	5	177	2	(20)
Untreated	12	0	(0)	9	370	3	(25)
RIP suppression of 8.5 × 10^7 SD							
SD+RIP	4	3	(75)	1	33	0	(0)
SD+saline	4	1	(25)	3	39	0	(0)
RIP suppression of 1.4 × 10^8 SD							
SD+RIP	8	4	(50)	4	45	0	(0)
SD+saline	6	0	(0)	6	100	0	(0)
RIP and Pep suppression of 1.4 × 10^9 SD							
SD+RIP	10	3	(30)	3	39	4	(40)
SD+saline	10	2	(20)	6	160	2	(20)
SD+Pep	10	9	(90)	1	56	0	(0)
SD+DMSO	9	2	(20)	4	128	3	(22)

N. Balaban, R. T. Nhan, S. Scott, R. M. Ridgley, R. Rasooly, J. R. Carlson, Department of Medical Pathology, University of California, Davis, CA 95616, USA.
T. Goldkorn and L. B. Dang, Department of Internal Medicine, University of California, Davis Medical Center, Davis, CA 95616, USA.
A. Rasooly, Department of Microbiology, University of Maryland, College Park, MD 20742, USA.
S. C. Wright and J. W. Larrick, Palo Alto Research Institute of Molecular Medicine, Mountain View, CA 94043, USA.

*To whom correspondence should be addressed. E-mail: nbalaban@ucdavis.edu